*nanomaterials*

MDPI

*Article*

# Thermal CO Oxidation and Photocatalytic $CO_2$ Reduction over Bare and M-$Al_2O_3$ (M = Co, Ni, Cu, Rh, Pd, Ag, Ir, Pt, and Au) Cotton-Like Nanosheets

**Hee Jung Yoon [1,†], Ju Hyun Yang [2,3,†], So Jeong Park [2] and Youngku Sohn [1,2,3,*]**

[1] Department of Chemistry, Yeungnam University, Gyeongsan 38541, Korea; hohoya0102@naver.com
[2] Department of Chemistry, Chungnam National University, Daejeon 34134, Korea; mil03076@naver.com (J.Y.); jsjs5921@naver.com (S.P.)
[3] Department of Chemical Engineering and Applied Chemistry, Chungnam National University, Daejeon 34134, Korea
* Correspondence: youngkusohn@cnu.ac.kr; Tel.: +82-42-821-6548
† These authors equally contributed to this work.

**Abstract:** Aluminum oxide ($Al_2O_3$) has abundantly been used as a catalyst, and its catalytic activity has been tailored by loading transition metals. Herein, $\gamma$-$Al_2O_3$ nanosheets were prepared by the solvothermal method, and transition metals (M = Co, Ni, Cu, Rh, Pd, Ag, Ir, Pt, and Au) were loaded onto the nanosheets. Big data sets of thermal CO oxidation and photocatalytic $CO_2$ reduction activities were fully examined for the transition metal-loaded $Al_2O_3$ nanosheets. Their physicochemical properties were examined by scanning electron microscopy, high-resolution transmission electron microscopy, X-ray diffraction crystallography, and X-ray photoelectron spectroscopy. It was found that Rh, Pd, Ir, and Pt-loading showed a great enhancement in CO oxidation activity while other metals negated the activity of bare $Al_2O_3$ nanosheets. Rh-$Al_2O_3$ showed the lowest CO oxidation onset temperature of 172 °C, 201 °C lower than that of bare $\gamma$-$Al_2O_3$. $CO_2$ reduction experiments were also performed to show that CO, $CH_3OH$, and $CH_4$ were common products. Ag-$Al_2O_3$ nanosheets showed the highest performances with yields of 237.3 ppm for CO, 36.3 ppm for $CH_3OH$, and 30.9 ppm for $CH_4$, 2.2×, 1.2×, and 1.6× enhancements, respectively, compared with those for bare $Al_2O_3$. Hydrogen production was found to be maximized to 20.7 ppm during $CO_2$ reduction for Rh-loaded $Al_2O_3$. The present unique pre-screening test results provided very useful information for the selection of transition metals on $Al_2O_3$-based energy and environmental catalysts.

**Keywords:** $\gamma$-$Al_2O_3$ nanosheets; transition metal-loading; CO oxidation; photocatalytic $CO_2$ reduction; physicochemical properties; hydrogen production

check for updates

**Citation:** Yoon, H.J.; Yang, J.H.; Park, S.J.; Sohn, Y. Thermal CO Oxidation and Photocatalytic $CO_2$ Reduction over Bare and M-$Al_2O_3$ (M = Co, Ni, Cu, Rh, Pd, Ag, Ir, Pt, and Au) Cotton-Like Nanosheets. *Nanomaterials* **2021**, *11*, 1278. https://doi.org/10.3390/nano11051278

Academic Editor: José M. Doña-Rodríguez

Received: 30 March 2021
Accepted: 9 May 2021
Published: 13 May 2021

## 1. Introduction

Aluminum oxide ($Al_2O_3$) has extensively been used as a heterogeneous catalyst in diverse catalytic reactions of CO oxidation [1–19], $CO_2$ reduction [20–23], $CO_2$ methanation/hydrogenation [20,24–27], and preferential oxidation of CO [28,29]. The efforts to increase the catalytic activity of the metal oxide have been devoted to the modification of the metal surface by loading of transition metals in groups of 9 (Co, Rh, and Ir), 10 (Ni, Pd, and Cu), and 11 (Cu, Ag, and Au). The morphology of a metal oxide support has also been a key factor for the enhancement of the catalytic activity [30]. It was reported that the role of an overlayer metal becomes different when the support metal oxide is different [2]. The relative catalytic activities of overlayer metals also become different when the catalytic application areas are different for the application to CO oxidation using transition metal-loaded $Al_2O_3$ catalysts.

Chen et al. prepared Pt nanoparticles (NPs) on $Al_2O_3$ and observed 100% CO conversion at −20 °C [1]. For the extremely high activity compared with a commercial Pt/$Al_2O_3$, based on the experimental and the density functional theory (DFT) calculations, they proposed that CO was initially adsorbed on Pt(OH) kink sites and reacted with OH to release gaseous $CO_2$. Afterward, OH was regenerated by activation of $O_2$ on terrace sites. Lou and Liu studied CO oxidation of single Pt atoms dispersed on $Fe_2O_3$ (highly reducible), ZnO (reducible), and $\gamma$-$Al_2O_3$ (irreducible) supports, and observed that the catalytic activity was in the order of Pt/$\gamma$-$Al_2O_3$ < Pt/ZnO < Pt/$Fe_2O_3$ [2], where the highly reducible support showed the highest catalytic activity. Chen et al. tested Pt/$Al_2O_3$ for preferential oxidation (PROX) of CO in $H_2$ [29]. They concluded that CO conversion and $CO_2$ selectivity reached up to 100% in a wide range of −30 °C to 120 °C. The high performance was attributed to a combination of Pt(OH) and metallic Pt on the $Al_2O_3$ support. Therefore, the adsorption of CO and the activation of $O_2$ were optimally tuned to maximize the performance. For monodispersed single Pt atoms on θ-$Al_2O_3$, Moses-DeBusk et al. found that the CO oxidation did not follow a conventional Langmuir-Hinshelwood mechanism [11]. The Pt atom was first oxygenated, and then CO was bound to form a carbonate ($CO_3$), which dissociated to generate gaseous $CO_2$ [11]. Yang et al. employed the DFT calculation to investigate the relative CO oxidation for single-atom catalysts of Ni/$\gamma$-$Al_2O_3$ and Pd/$\gamma$-$Al_2O_3$ [7]. They reported that Ni showed an unexpectedly higher CO oxidation activity than the Pd. Ananth et al. synthesized $Ag_2O$/$\gamma$-$Al_2O_3$ and ($Ag_2O$ + $RuO_2$)/$\gamma$-$Al_2O_3$ catalysts and tested the CO oxidation performances to show that the catalytic activity was increased by the addition of $RuO_2$ [6]. Han et al. reported a high CO oxidation activity at 30 °C for NiO ($\leq$1 nm) on mesoporous $Al_2O_3$ prepared using atomic layer deposition [16]. The deactivation was found to be lowered with increasing the pre-annealing temperature.

For the application of $Al_2O_3$ to $CO_2$ reduction, Zhao et al. synthesized Au/$Al_2O_3$/$TiO_2$ nanocomposites, where the atomic-layer $Al_2O_3$ was sandwiched between the two layers [21]. They tested the photocatalytic $CO_2$ reduction activity and observed CO (major) and $CH_4$ (minor) as products. It was concluded that the charge transfer and surface charge recombination were highly influenced by $Al_2O_3$ interlayer thickness. Therefore, the maximum photocatalytic activity (37 μmol/g of CO and 2 μmol/g of $CH_4$) was obtained by achieving optimum $Al_2O_3$ thickness (5 Å). Kwak et al. performed a temperature-programmed $CO_2$ reduction with $H_2$ on Ru/$Al_2O_3$ catalysts and observed CO and $CH_4$ formation yields with activation energies of 82 kJ/mol and 62 kJ/mol, respectively [20]. It was found that CO formation selectivity was increased with increasing Ru metal dispersion but decreased with increasing Ru clustering and concluded that CO was not an intermediate species for $CH_4$ formation. Chein and Wang tested $CO_2$ methanation activities using Ni/$Al_2O_3$, Ru/$Al_2O_3$, and Ru-Ni/$Al_2O_3$ catalysts [27] and found that the hybrid bimetallic Ru-Ni showed higher performance than the monometallic catalysts.

Although numerous detailed in-depth studies have been performed using transition metal-loaded $Al_2O_3$ catalysts, no systematic comparison studies have been reported among diverse (M = Co, Ni, Cu, Rh, Pd, Ag, Ir, Pt, and Au) transition metal-loaded $Al_2O_3$ catalysts prepared by the same synthesis method. Motivated by this, we synthesized transition metal-loaded $Al_2O_3$ nanosheets and evaluated thermal CO oxidation activity as well as photocatalytic $CO_2$ reduction activity. Consequently, the roles of overlayer transition metals were comparatively investigated in two totally different application reactions. Thereby, the present pre-screening test results provided useful information on the quick-selection of catalysts for thermal CO oxidation and photocatalytic $CO_2$ reduction.

## 2. Materials and Methods

### 2.1. Catalysts Synthesis Procedures

For the synthesis of Al precursor nanosheets, 1 mmol of aluminum nitrate nonahydrate ($Al(NO_3)_3$ $9H_2O$, 98%, Sigma-Aldrich, St. Louis, MO, USA), 0.008 g of polyethylene glycol (PEG, $M_n$ = 4000, Sigma-Aldrich, St. Louis, MO, USA), and 20 μL of oleic acid ($\geq$99%, Sigma-Aldrich, St. Louis, MO, USA) were fully dissolved by magnetic stirring in a mixed solvent of 10 mL of deionized water and 15 mL of ethanol (99.9%, Samchun Chem., Gyounggi, Korea) for 20 min. After that, the solution was transferred into a Teflon-lined stainless-steel autoclave reactor, which was then tightly capped for sealing. The tightly capped reactor was placed in an oven setting at 200 °C for 12 h. After the thermal reaction, the reactor was naturally cooled to room temperature, and the finally obtained white precipitates were collected by washing with deionized water and ethanol repeatedly by centrifugation at 3600 rpm. The collected wet powder was fully dried in an oven setting at 80 °C for 24 h. To obtain $Al_2O_3$ nanosheets, the dried powder sample was thermally annealed at 600 °C for 2 h.

For transition metal (M = Co, Ni, Cu, Rh, Pd, Ag, Ir, Pt, and Au) loadings, 50 mg of $Al_2O_3$ nanosheets were fully dispersed in 20 mL ethanol, followed by adding 2 mol% of metal ions. The chemicals for metal ions were cobalt(II) nitrate hexahydrate ($\geq$98%, Sigma-Aldrich, St. Louis, MO, USA), nickel(II) nitrate hexahydrate ($\geq$98.5%, Sigma-Aldrich, St. Louis, MO, USA), copper(II) nitrate trihydrate (99%, Daejung, Gyounggi, Korea), rhodium(III) chloride hydrate ($\geq$99.9%, Sigma-Aldrich, St. Louis, MO, USA), palladium(II) chloride (99.8%, Sigma-Aldrich, St. Louis, MO, USA), silver nitrate solution (0.1 N, Samchun Pure Chem., Gyounggi, Korea), platinum (III) chloride ($\geq$99.9%, Sigma-Aldrich, St. Louis, MO, USA), iridium (III) chloride hydrate ($\geq$99.9%, Sigma-Aldrich, St. Louis, MO, USA), and gold(III) chloride trihydrate ($\geq$99.9%, Sigma-Aldrich, St. Louis, MO, USA). After complete mixing, the solvent was slowly evaporated by gentle heating (50 °C) while stirring. The dried M-loaded $Al_2O_3$ nanosheets were, again, thermally annealed at 600 °C for 2 h.

### 2.2. Sample Characterization

The surface morphologies of the Al-precursor, $Al_2O_3$ nanosheets, and M-loaded $Al_2O_3$ nanosheets were examined using a scanning electron microscope (SEM, Hitachi S-4800, Hitach Ltd., Tokyo, Japan) at conditions of 10 kV and 10 mA. X-ray crystallographic diffraction patterns were recorded using a PANalytical X'Pert Pro MPD diffractometer (PANalytical, Almelo, Netherland) with Cu K$\alpha$ radiation (40 kV and 30 mA). Transmission electron microscopic (TEM) and high-resolution TEM (HRTEM) were obtained for bare $Al_2O_3$ nanosheets and the selected Ni- and Rh-loaded $Al_2O_3$ nanosheets using an FEI Tecnai G2 F20 TEM (Hillsboro, OR, USA) operated at 300.0 kV. X-ray photoelectron spectra were taken using a Thermo-VG Scientific K-alpha$^+$ spectrometer (Thermo VG Scientific, Waltham, MA, USA) with a hemispherical energy analyzer. Attenuated total reflection Fourier-transform infrared spectroscopy (FT-IR) was employed using a Nicolet iS 10 FT-IR spectrometer (Thermo Scientific Korea, Seoul, Korea). The Brunauer-Emmett-Teller (BET) surface areas were measured using a ChemBET TPR/TPD analyzer (Quantachrome Instruments Corp., Boynton Beach, FL, USA) equipped with a thermal conductivity detector.

### 2.3. Thermal CO Oxidation and Photocatalytic $CO_2$ Reduction Experiments

For thermal CO oxidation reactions, 20 mg of a catalyst was initially loaded into a U-shape quartz tube. After that, the tube was positioned in a temperature-programmed furnace. The temperature heating rate was 20 °C/min, and the flowing gas was CO(1.0%)/$O_2$(2.5%)/$N_2$ at a flow rate of 40 mL/min. The gas products from the outlet of the tube were monitored using a quadrupole mass spectrometer (RGA200, Stanford Research Systems, Sunnyvale, CA, USA). After the first run to a maximum temperature of 500 °C, the sample cell was naturally cooled to a room temperature of 25 °C. After that, the second run was performed at room temperature.

For photocatalytic $CO_2$ reduction experiments, 3 mg of a catalyst was fully dispersed on a quartz disc (an area of 15.9 $cm^2$) and placed in a stainless-steel reactor (volume ~40 mL) with additional deionized water (20 µL) beside the disc. After that, the reactor was tightly closed with a quartz window (0.3 cm thick and 4.5 cm diameter) on top. Afterward, pure (99.999%) $CO_2$ gas was fully flushed and filled with the gas. For the photocatalytic $CO_2$ reduction test, the reactor with the quartz window was placed under UVC (200–280 nm) lamps (a power density of 5.94 mW/$cm^2$) for 12 h. After the UVC irradiation time, 0.5 mL of gas was taken and injected into a YL 6500 gas chromatograph (GC, Young In Chromass

Co., Ltd., Seoul, Korea). For the analysis of the CO, $CH_3OH$, $CH_4$, and $H_2$ products, the GC system was equipped with HP-Plot Q-PT column (Agilent Technologies, Inc., Santa Clara, CA, USA), 40/60 Carboxen-1000 column (Sigma-Aldrich, St. Louis, MO, USA), a Ni catalyst methanizer assembly, a thermal conductivity detector, and a flame ionization detector.

## 3. Results and Discussion

Figure 1(a,a1) show the SEM image of the as-prepared Al-precursor with a morphology of cotton-like nanostructures. Figure 1b shows the sample after thermal annealing at 600 °C, abbreviated as bare $Al_2O_3$. It appears that the morphology showed no significant change, but the nanosheets became somewhat compacted. The Brunauer-Emmett-Teller (BET) surface area of bare $Al_2O_3$ was measured to be 154.4 $m^2/g$. The corresponding transmission electron microscope (TEM) image clearly showed the morphology of nanosheets. For the high-resolution TEM image of bare $Al_2O_3$, clear lattice fringes were seen, and the lattice spacing was estimated to be 0.197 nm. This was well-matched to the (002) crystal plane of cubic phase gamma-$Al_2O_3$. This was further discussed in detail below. The structure projection of the (002) and (022) planes for $Al_2O_3$ are shown in Figure 1(b1) for visual understanding.

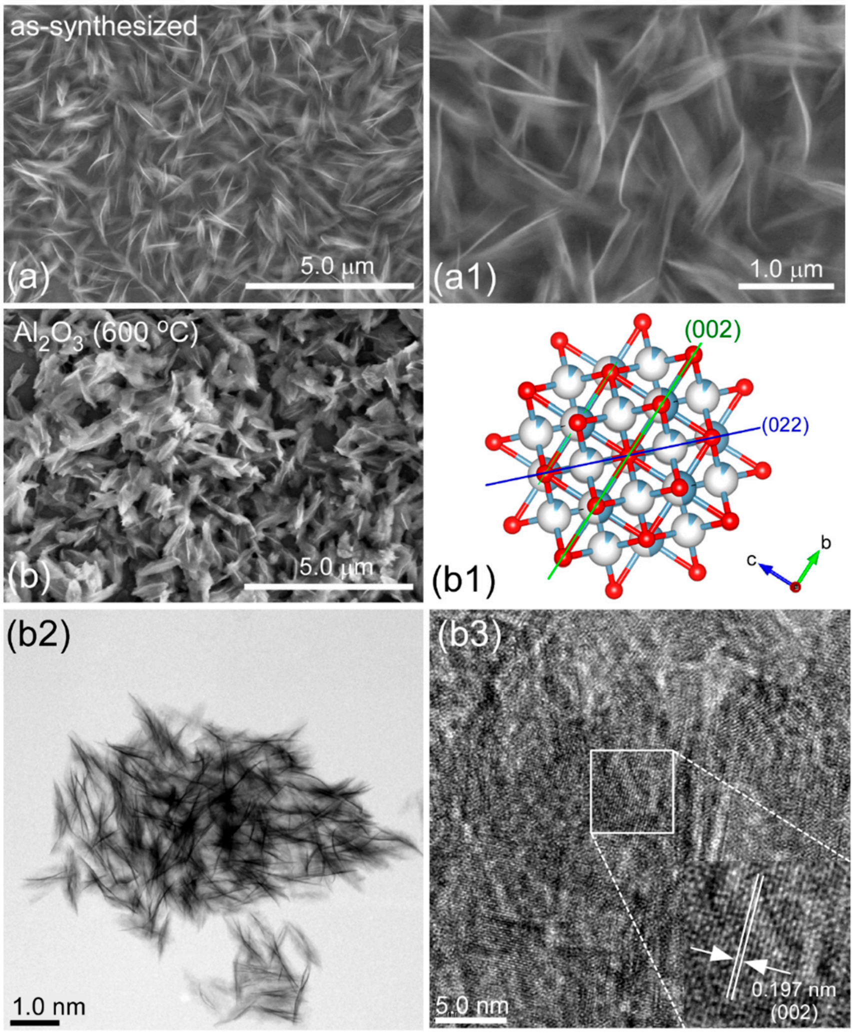

**Figure 1.** Scanning electron microscope (SEM) (**a**,**a1**,**b**), transmission electron microscope (TEM) (**b2**), high resolution TEM (**b3**) images of the as-synthesized Al-precursor (**a**,**a1**) and $Al_2O_3$ (**b**,**b2**,**b3**), and the structure projection (**b1**) of the (002) and (022) planes for cubic phase $\gamma$-$Al_2O_3$.

Figure 2 shows the SEM and TEM images of selected Ni- and Rh-loaded $Al_2O_3$ nanosheets. The SEM images of other M-loaded $Al_2O_3$ nanosheets are provided in the Supporting Information, Figure S1. The SEM image (Figure 2a) of Rh-$Al_2O_3$ showed small nanoparticles embedded on the nanosheets. The nanoparticles appeared as a result of Rh particle formation. The color of burlywood was clearly different from the white color for bare $Al_2O_3$. On the other hand, the SEM image (Figure 2b) of Ni-$Al_2O_3$ nanosheets showed only cotton-like nanosheets. It was difficult to discriminate Ni species from the bare $Al_2O_3$ support. However, the color clearly changed from white to pale blue upon Ni-loading. The photos and optical microscope images of the M-loaded $Al_2O_3$ nanosheets are provided in the Supporting Information, Figures S2 and S3, respectively. Although the SEM images showed no clear metal embedment, the color change was a clear indication of metal-loading on the $Al_2O_3$ support. The metal-loading was also confirmed by the X-ray photoelectron spectroscopy (XPS) data, discussed below.

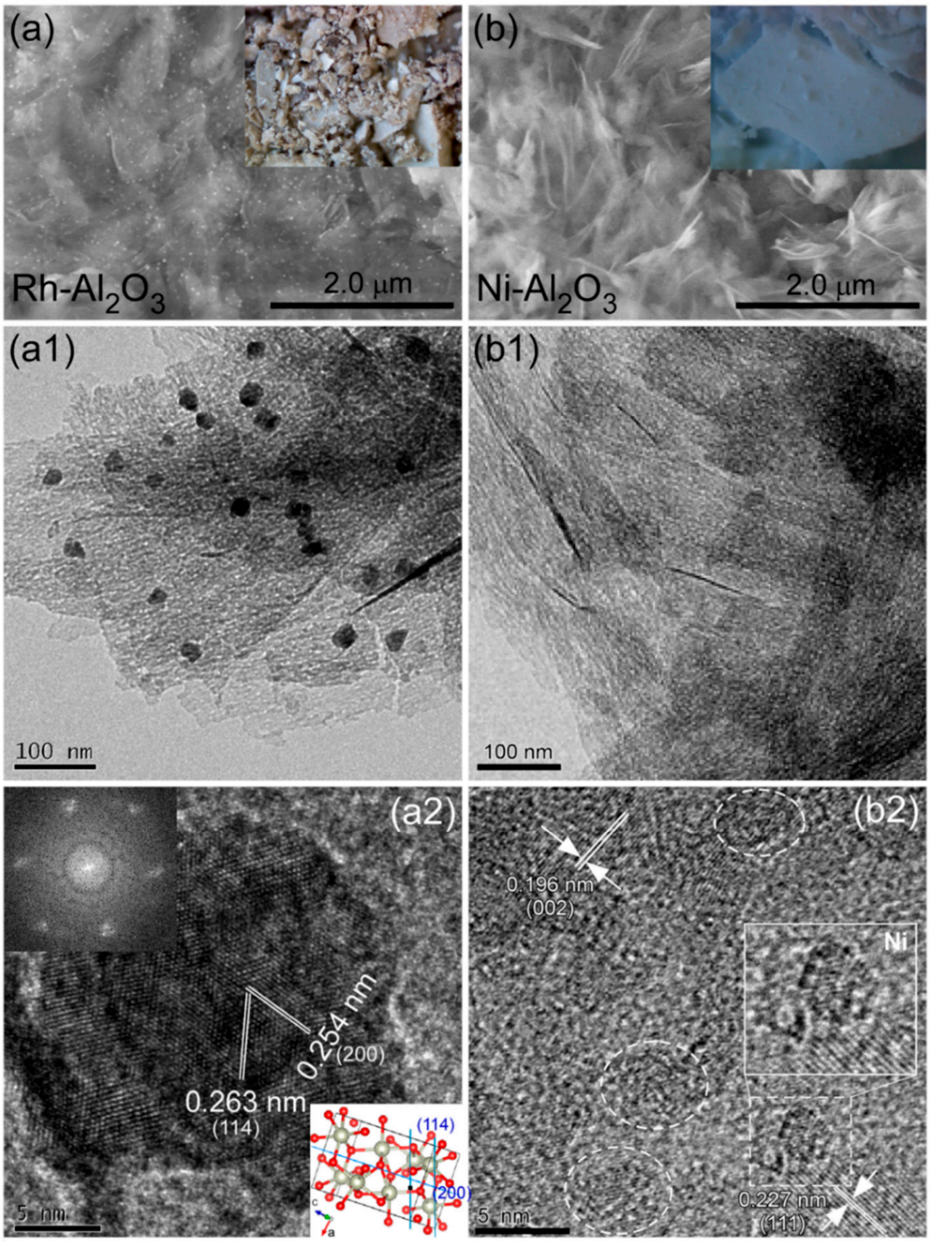

**Figure 2.** SEM (**a**,**b**), TEM (**a1**,**b1**), HRTEM (**a2**,**b2**) images of selected Rh-$Al_2O_3$ (**a**,**a1**,**a2**) and Ni-$Al_2O_3$ (**b**,**b1**,**b2**) nanosheets. Insets of Figure 2(a2) show the fast Fourier transform (FFT) pattern of the HRTEM image, and the structure projection of the (114) and (200) planes for $Rh_2O_3$.

The TEM images (Figure 2(a1)) of Rh-$Al_2O_3$ clearly showed NPs (with a size of ~20 nm) embedded onto the nanosheets. For the HRTEM image (Figure 2(b2)) of an Rh-NP, clear lattice fringes were observed, and the distances were estimated to be 0.263 nm and 0.254 nm. These distances matched well with the (114) and (200) crystal planes of orthorhombic (Pbca) $Rh_2O_3$ (ICSD ref. 98-000-9206), respectively. This indicated that Rh was embedded not in the metallic form but rather in the oxide form. This was further confirmed by the XPS data below. The fast Fourier transform (FFT) pattern of the HRTEM image reflected the crystallinity of the Rh oxide. The TEM images (Figure 2(b1)) of Ni-$Al_2O_3$ nanosheets showed only nanosheet morphology, consistent with the corresponding SEM image (Figure 2b).

For the HRTEM image in Figure 2(b2), the lattice fringes with distances of 0.227 nm and 0.196 nm matched well with the (111) and (002) crystal planes of the cubic phase $\gamma$-$Al_2O_3$. The lattices showed poor crystallinity compared with those of bare $Al_2O_3$, seen in Figure 1(b3). Interestingly, some areas (dotted circles) showed very poor crystallinity, and these appeared like amorphous particles. This is likely an indication of Ni embedment on the $Al_2O_3$ nanosheets. Very similarly for Co-$Al_2O_3$ nanosheets, although particles were not clearly seen in the TEM image (Supporting Information, Figure S4), the corresponding HRTEM image showed the areas with very poor crystallinity. The areas appeared like Co-embedment in the $Al_2O_3$ support.

The BET surface areas of Ni-$Al_2O_3$ and Rh-$Al_2O_3$ nanosheets were measured to be 151.2 $m^2/g$ and 153.8 $m^2/g$, respectively. The surface areas were very similar to that of bare $Al_2O_3$. This indicated that the surface area was not significantly impacted by the metal-loading.

Figure 3 displays the X-ray diffraction patterns of bare $Al_2O_3$ and M-loaded $Al_2O_3$ nanosheets. For the XRD patterns of bare $Al_2O_3$, two distinctive peaks were observed at $2\theta = 45.9°$ and 67.0°. These two peaks could be assigned to the (002) and (022) planes of cubic phase (Fm-3m) $\gamma$-$Al_2O_3$, (ICSD ref. 98-003-0267), respectively. The XRD result was in good consistency with the HRTEM result of the bare $Al_2O_3$ nanosheet. For the XRD profiles of M-loaded $Al_2O_3$ nanosheets, two peaks were commonly observed, as expected. Interestingly, Co, Ni, Cu, Rh, and Ag-loaded samples showed no significant extra peaks in the corresponding XRD profiles. These results indicated that the metals were loaded with an amorphous oxide state (discussed below in XPS) or embedded very uniformly without forming good crystal phases. In addition, because the metal amount was only 2 mol%, the XRD patterns could not be clearly observed when the phase was an amorphous oxide form. As seen in the HRTEM images of Ni-$Al_2O_3$ and Co-$Al_2O_3$ nanosheets discussed above (Figure 2(b2) and Figure S4, respectively), the particle-like areas showed very poor crystallinity. On the other hand, Pd, Ir, Pt, and Au-loaded samples showed new peaks in the corresponding XRD profiles.

For the XRD patterns of Pd-$Al_2O_3$ nanosheets, several peaks at $2\theta = 33.8°$, 42.0°, 54.7°, 60.1°, and 71.5° showed good matches with the (011), (110), (112), (013), and (121) crystal planes of tetragonal (p 42/mmc) PdO (ICSD ref. 98-002-9281), respectively [13]. For Ir-$Al_2O_3$ nanosheets, several strong XRD peaks were observed at $2\theta = 27.9°$, 34.6°, 39.9°, 53.9°, 57.9°, 58.3°, 66.0°, 69.0°, and 73.0°, with good matches with the (110), (011), (020), (121), (220), (002), (130), (112), and (031) crystal planes of tetragonal (p 42/mnm) $IrO_2$ (ICSD ref. 98-008-4577), respectively. For Pt-$Al_2O_3$ nanosheets, three major peaks were observed at $2\theta = 39.8°$, 46.2°, and 67.5°, assigned to the (111), (002,) and (022) crystal planes of the cubic (Fm-3m) crystal phase of metallic Pt (ICSD ref. 98-007-6153), respectively. For Au-$Al_2O_3$ nanosheets, three strong peaks were observed at $2\theta = 38.1°$, 44.3°, and 64.5°, assigned to the (111), (002), and (022) crystal planes of the cubic (Fm-3m) crystal phase of Au (ICSD ref. 98-061-1624), respectively.

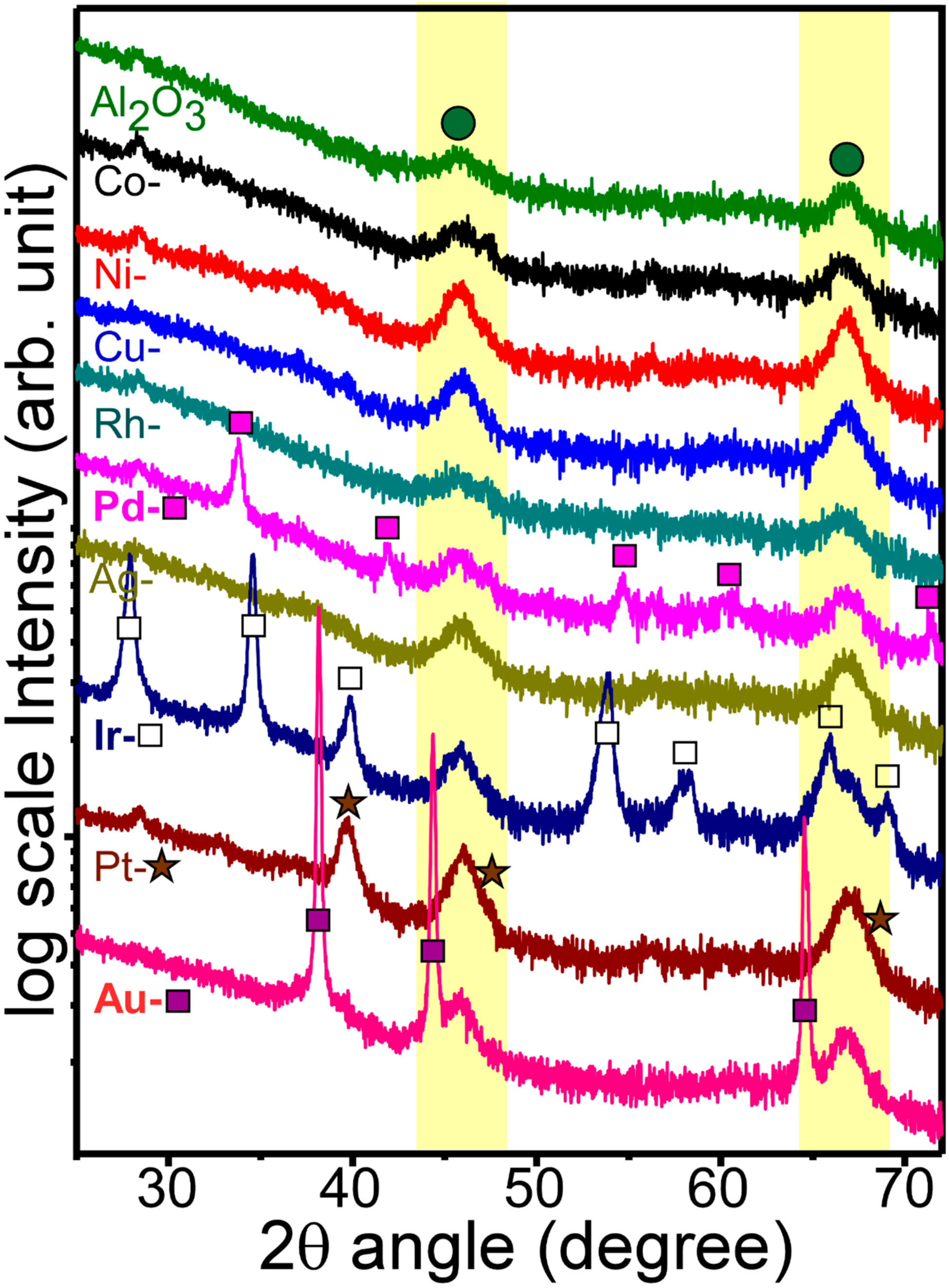

**Figure 3.** XRD profiles bare $Al_2O_3$ and M-loaded $Al_2O_3$ nanosheets.

XPS was employed to confirm the loading of the transition metals and examine the oxidation states. Figure 4 shows Co 2p, Ni 2p, Cu 2p, Rh 3d, Pd 3d, Ag 3d, Ir 4d, Pt 4d, and Au 4d of Co-$Al_2O_3$, Ni-$Al_2O_3$, Cu-$Al_2O_3$, Rh-$Al_2O_3$, Pd-$Al_2O_3$, Ag-$Al_2O_3$, Ir-$Al_2O_3$, Pt-$Al_2O_3$, and Au-$Al_2O_3$ nanosheets, respectively. XPS valence band spectra (Figure 4, right panel) are also displayed for the corresponding samples. The survey, Al 2p, O 1s, and C 1s profiles are provided in the Supporting Information, Figure S5. All the binding energies (BEs) were referenced to the C 1s XPS peak at 284.8 eV. The survey spectra commonly showed the elements of Al, O, and C (surface impurities), as expected. The XPS peaks of the loaded transition metals were very weakly observed.

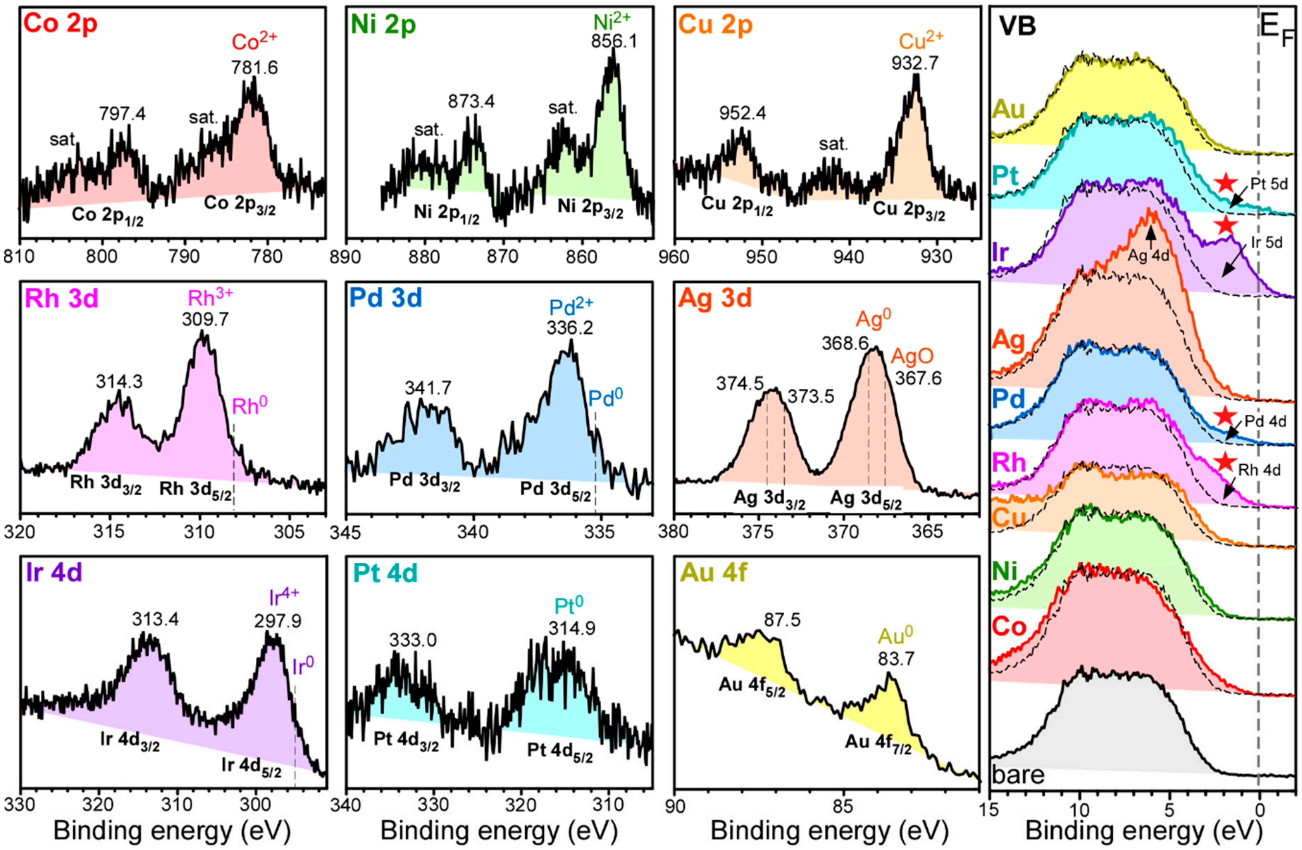

**Figure 4.** Co 2p, Ni 2p, Cu 2p, Rh 3d, Pd 3d, Ag 3d, Ir 4d, Pt 4d, Au 4d, and VB profiles of Co-$Al_2O_3$, Ni-$Al_2O_3$, Cu-$Al_2O_3$, Rh-$Al_2O_3$, Pd-$Al_2O_3$, Ag-$Al_2O_3$, Ir-$Al_2O_3$, Pt-$Al_2O_3$, and Au-$Al_2O_3$ nanosheets.

For Co-$Al_2O_3$ nanosheets, Co $2p_{1/2}$ and Co $2p_{3/2}$ XPS peaks were observed at binding energies (BEs) of 797.4 eV and 781.6 eV, respectively, with a spin-orbit splitting of 15.8 eV. This could be attributed to $Co^{2+}$ of CoO and $Co(OH)_2$ [31,32]. The corresponding satellite peaks for $Co^{2+}$ were clearly observed around 803 eV and 786 eV. For Ni-$Al_2O_3$ nanosheets, Ni $2p_{1/2}$ and Ni $2p_{3/2}$ XPS peaks were observed at binding energies (BEs) of 873.4 eV and 856.1 eV, respectively, with a spin-orbit splitting of 17.3 eV. This could be attributed to $Ni^{2+}$ of NiO and $Ni(OH)_2$ [15,31,32]. The corresponding satellite peaks for $Ni^{2+}$ were clearly observed around 880 eV and 862 eV. For Cu-$Al_2O_3$ nanosheets, Cu $2p_{1/2}$ and Cu $2p_{3/2}$ XPS peaks were observed at binding energies (BEs) of 952.4 eV and 932.7 eV, respectively, with a spin-orbit splitting of 19.7 eV. This could be attributed to $Cu^{2+}$ of CuO and $Cu(OH)_2$ [32,33]. The corresponding satellite peak for $Cu^{2+}$ was clearly observed around 942 eV. For Co, Ni, and Cu, no metallic XPS peaks were observed. On the basis of XRD, HRTEM, and XPS data, Co, Ni, and Cu appeared to be embedded as an amorphous oxide form.

For Rh-$Al_2O_3$ nanosheets, Rh $3d_{3/2}$ and Rh $3d_{5/2}$ XPS peaks were observed at BEs of 314.3 eV and 309.7 eV, respectively, with a spin-orbit splitting of 4.6 eV. The XPS BEs were attributed to an oxidation state of $Rh^{3+}$ [32,34]. As discussed above, the lattice distances in the HRTEM image confirmed orthorhombic $Rh_2O_3$. An additional weak shoulder peak was seen around 308 eV for Rh $3d_{5/2}$ peak. This could be due to metallic Rh [32,34]. On the basis of the XPS and HRTEM data, Rh-species appeared to be consistent with Rh@$Rh_2O_3$ core-shell type structure.

For Pd-$Al_2O_3$ nanosheets, Pd $3d_{3/2}$ and Pd $3d_{5/2}$ XPS peaks were observed at BEs of 341.7 eV and 336.2 eV, respectively, with a spin-orbit splitting of 5.5 eV. The XPS peaks were attributed to an oxidation state of $Pd^{2+}$ [32,34,35]. There was a good coincidence between the oxidation state of the XPS and the XRD profiles of tetragonal PdO. A weak shoulder of the Pd $3d_{5/2}$ peak was seen around 335.5 eV, plausibly due to metallic Pd [32]. For Ag-$Al_2O_3$ nanosheets, Ag $3d_{3/2}$ and Ag $3d_{5/2}$ XPS peaks were observed at BEs of 374.5 eV and 368.6 eV, respectively. This was attributed to metallic Ag [6,32,36]. The shoulder XPS peak at 367.6 eV for Ag $3d_{5/2}$ was plausibly due to AgO [36]. On the basis of the XPS profile for each M-$Al_2O_3$ sample, it could be concluded that the transition metal was loaded on the $Al_2O_3$ support.

For Ir-$Al_2O_3$ nanosheets, Ir $4d_{3/2}$ and Ir $4d_{5/2}$ XPS peaks were observed at BEs of 313.6 eV and 297.7 eV, respectively. These peaks were assigned to the $Ir^{4+}$ oxidation state [37], in good coincidence with the XRD profiles of tetragonal $IrO_2$, shown above. A weak shoulder of Ir $4d_{5/2}$ peak was seen around 295 eV, plausibly due to metallic Ir [37]. For Pt-$Al_2O_3$ nanosheets, Pt $4d_{3/2}$ and Pt $4d_{5/2}$ XPS peaks were observed at BEs of 332.9 eV and 314.9 eV, respectively, with a spin-orbit splitting of 18.0 eV. The XPS peaks were attributed to metallic Pt [34,35], which was well-fitting with the XRD result of metallic Pt. For Au-$Al_2O_3$ nanosheets, the Au $4f_{7/2}$ and Au $4f_{5/2}$ XPS peaks were observed at BEs of 87.3 eV and 83.6 eV, respectively, with a spin-orbit splitting of 3.7 eV. The XPS peaks were attributed metallic Au [32]. This result was in good agreement with the XRD profiles of metallic Au, shown above.

For the Al 2p XPS profiles (Supporting Information, Figure S5), a broad peak was commonly observed around 74.1 eV, attributed to Al of the $Al_2O_3$ support [32,38]. An additional peak at 75.0 eV was observed and attributed to the Al of surface Al-OH species [32,38]. For the O 1s XPS profiles (Supporting Information, Figure S5), a broad peak was commonly observed around 530.9 eV due to lattice O of $Al_2O_3$ support. A broad shoulder at 532.5 eV was attributed to oxygen defects and surface $OH/H_2O$ species [39].

The valence band (VB) spectra are shown in Figure 4 to further examine electronic structures. For the VB of bare $Al_2O_3$ nanosheets, two broad features were seen around 9 eV and 6 eV, attributed bonding $2p\sigma$ (mixed with Al 3s, Al 3p, and Al 3d) and antibonding $2p\pi$ of the oxygen [40]. For VB spectra of M-$Al_2O_3$ nanosheets, the density of states (DOS) was observed to be closer to the Fermi level. Especially, Rh, Pd, Ir, and Pt showed more clearly new features near 2 eV below the Fermi level, attributed to the Rh 4d, Pd 4d, Ir 5d, and Pt 5d, respectively. This could be related to the higher CO oxidation activities for these metals, discussed below. However, the DOS profiles showed no explicit relationship with the photocatalytic $CO_2$ reduction activity. The detailed roles of the overlayer elements could be understood with the aid of density functional theory.

Temperature-programmed CO oxidation profiles (Supporting Information, Figure S6) were obtained to examine thermal CO oxidation catalytic activities for bare $Al_2O_3$ and M-$Al_2O_3$ nanosheets. To evaluate the catalytic activities of the catalysts, Figure 5a,b display the CO oxidation onset temperatures for the first and the second runs, respectively. Table 1 summarizes the onset temperatures ($T_{\text{M-Al2O3,onset}}$) and the temperature difference ($T_{\text{M-Al2O3,2nd}} - T_{\text{M-Al2O3,1st}}$) between the first and the second runs. The onset temperatures of Ir-, Pt-, Pd-, and Rh-loaded $Al_2O_3$ nanosheets were observed to be much lower than those of Au-, Ag-, Cu-, Co-, and Ni-loped $Al_2O_3$ nanosheets. The group 11 (Au, Ag, and Cu) and the period 4 (Co, Ni, and Cu) elements showed much poor catalytic activity on the $Al_2O_3$ support. Additionally, the onset temperatures of Au and Ag-loaded $Al_2O_3$ nanosheets were unexpectedly even higher than expected [6,10,15]. In other words, the Au- and Ag-loaded $Al_2O_3$ nanosheets showed poorer CO oxidation activity. In the first run, the Rh-$Al_2O_3$ nanosheets showed the lowest onset of 135 °C, while the Ni-$Al_2O_3$ nanosheets showed the highest onset of 490 °C. The temperature difference between the two samples was estimated to be 335 °C. In the second run, the Rh-$Al_2O_3$ nanosheets also showed the lowest onset of 172 °C while the Ni-$Al_2O_3$ nanosheets showed the highest onset of 480 °C. The temperature difference was estimated to be 308 °C. Pd, Ir, and Pt showed the CO oxidation onsets at 207 °C, 217 °C, and 216 °C, respectively, in the second run. For highly dispersed (or single atom state) 0.2 wt % Pt on mesoporous $Al_2O_3$ support, Zhang et al. reported CO oxidation onset at ~200 °C, which was in good coincidence with the present result [5]. These results clearly indicated that the CO oxidation activity was highly influenced by the nature of overlayer metal species.

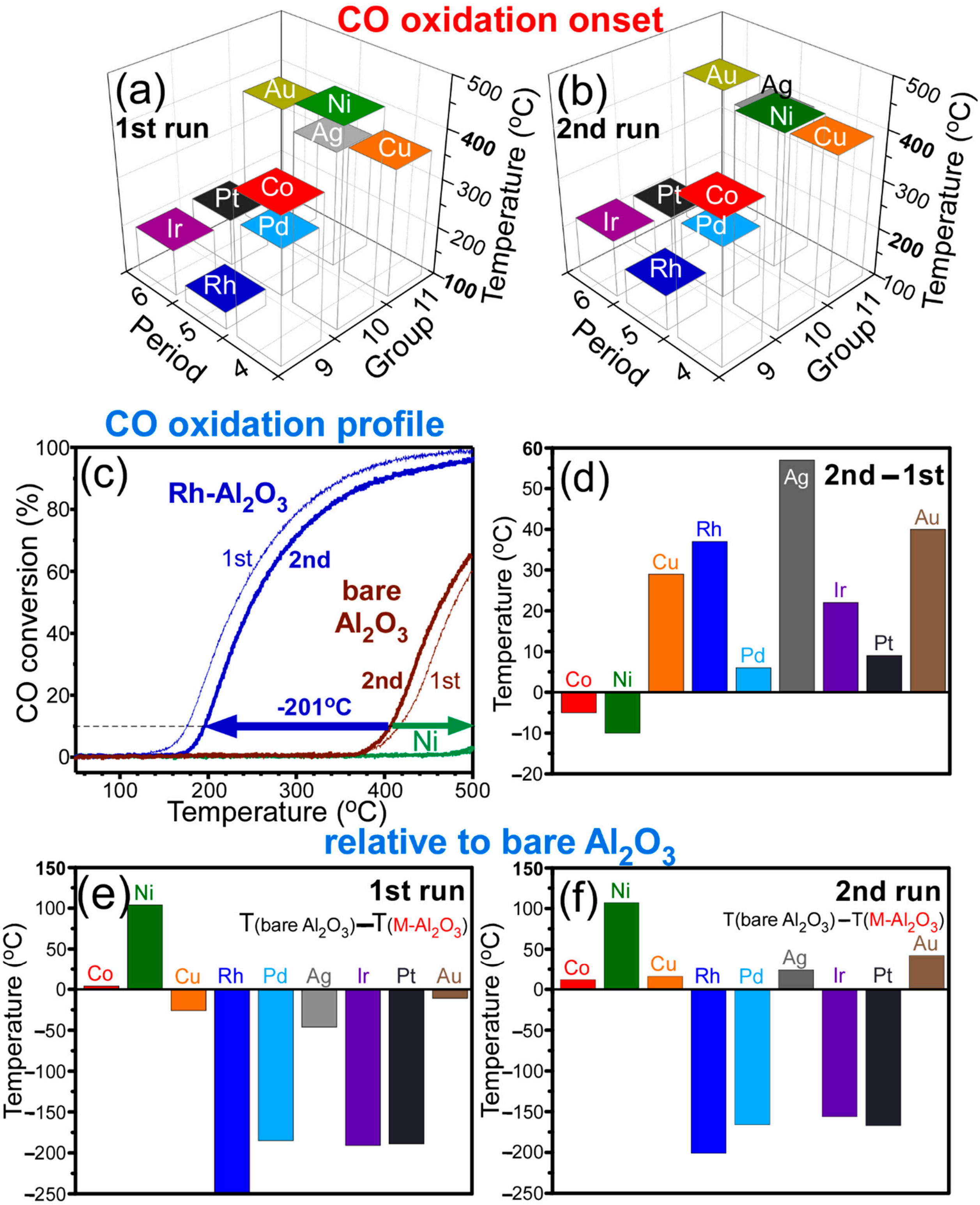

**Figure 5.** CO oxidation onsets for the first (**a**) and second (**b**) runs of M-loaded $Al_2O_3$ nanosheets. Selected first and second run CO oxidation profiles with temperature (**c**) for bare, Rh- and Ni-$Al_2O_3$ nanosheets. Differences in CO oxidation onsets for the first and the second runs (**d**) and relative CO oxidation onset temperatures relative to that of bare nanosheets (**e**,**f**).

**Table 1.** CO oxidation onset temperatures ($T_{\text{M-Al2O3,onset}}$) in the first and second runs. Differences in CO oxidation onset temperatures ($T_{\text{M-Al2O3,2nd}} - T_{\text{M-Al2O3,1st}}$) between the first and second runs.

| Group #9 | First Run | Second Run | Diff. | Group #10 | First Run | Second Run | Diff. | Group #11 | First Run | Second Run | Diff. |
|---|---|---|---|---|---|---|---|---|---|---|---|
| Co | 390 | 385 | −5 | Ni | 490 | 480 | −10 | Cu | 360 | 389 | 29 |
| Rh | 135 | 172 | 37 | Pd | 201 | 207 | 6 | Ag | 340 | 397 | 57 |
| Ir | 195 | 217 | 22 | Pt | 197 | 206 | 9 | Au | 375 | 415 | 40 |

Figure 5c shows the CO oxidation profiles for the first and the second runs of the selected samples (bare $Al_2O_3$, Ni-$Al_2O_3$, and Rh-$Al_2O_3$ catalysts). As seen in the Figure 5, the CO oxidation onset of Rh-$Al_2O_3$ occurred much earlier than that of bare $Al_2O_3$. The onsets of Rh-$Al_2O_3$ in the first and the second runs were observed to be 251 °C and 201 °C lower than those of bare $Al_2O_3$, respectively. However, the onset temperatures became much higher upon loading Ni.

To examine the difference in catalytic activity between the first and the second runs, Figure 5d plots the temperature differences ($T_{\text{M-Al2O3,2nd}} - T_{\text{M-Al2O3,1st}}$) in the CO oxidation onsets between the first and the second runs. In the first run, the CO oxidation reactions were performed with the as-prepared samples. In the second run, the CO oxidation reactions were performed with samples, which were already participated in the first run. Therefore, the surface states (or the catalytic-active sites) were expected to be different for the samples in the first and the second runs. The values ($T_{\text{M-Al2O3,2nd}} - T_{\text{M-Al2O3,1st}}$) are summarized in Table 1. The positive value (Figure 5d) indicated that the CO oxidation started at a higher temperature in the second run. In other words, the CO oxidation catalytic activity became lower in the second run.

For Co- and Ni-$Al_2O_3$ nanosheets, the onset temperatures in the second run were observed to be slightly lower than those in the first run. However, the other samples commonly showed higher onset temperatures in the second run, compared with the first run. This indicated that, for the latter, the catalytic activity became somewhat lower after the first run. The lower catalytic activity appeared to be mainly due to a change in crystallinity and lower catalytic-active sites.

To evaluate the roles of the transition metals in catalytic activities, compared with bare $Al_2O_3$, Figure 5e,f show the relative CO oxidation onsets ($T_{Al_2O_3} - T_{\text{M-}Al_2O_3}$), compared with those of the first and the second runs of the bare $Al_2O_3$, respectively. The values are summarized in Table 2. In the first runs, the $T_{\text{Al2O3,1st}} - T_{\text{M-Al2O3,1st}}$ values of Co and Ni showed positive, and others showed negative values. In the second runs, Co, Ni, Cu, Ag, and Au showed positive, and others showed negative values. On the basis of Figure 5e,f, the catalytic activity became poorer upon loading Co and Ni, compared with bare $Al_2O_3$. Unexpectedly, the Au, Ag, and Cu (group 11) showed somewhat higher activities in the first run but showed poorer catalytic activity in the second run, compared with the bare $Al_2O_3$ nanosheet. The Rh, Pd, Ir, and Pt showed much higher (with lowering of onset temperatures between 156 °C and 261 °C) CO oxidation activity in the first and second runs. Conclusively, the CO oxidation activity showed the order of Ni < Co < Au < Cu < Ag < Pd < Pt < Ir < Rh in the first run, and Ni < Au < Ag < Cu < Co < Ir < Pt ≈ Pd < Rh in the second run.

**Table 2.** Differences in CO oxidation onset temperatures ($T_{\text{Al2O3,onset}} - T_{\text{M-Al2O3,onset}}$) in the first and second runs, compared with that of bare $Al_2O_3$ nanosheets. The CO oxidation onset temperatures of bare $Al_2O_3$ were 386 °C and 373 °C for the first and the second runs, respectively.

| Group #9 | First Run | Second Run | Group #10 | First Run | Second Run | Group #11 | First Run | Second Run |
|---|---|---|---|---|---|---|---|---|
| Co | 4 | 12 | Ni | 104 | 107 | Cu | −26 | 16 |
| Rh | −251 | −201 | Pd | −185 | −166 | Ag | −46 | 24 |
| Ir | −191 | −156 | Pt | −189 | −167 | Au | −11 | 42 |

For CO oxidation, a simplified mechanism is described below;

$$\text{M-Al}_2\text{O}_3 + \text{CO (g)} \rightarrow \text{CO(ad)-M-Al}_2\text{O}_3 \qquad \text{adsorption of CO} \tag{1}$$

$$\text{M-Al}_2\text{O}_3 + 1/2\text{O}_2\text{ (g)} \rightarrow \text{O(ad)-M-Al}_2\text{O}_3 \qquad \text{dissociative adsorption of O}_2 \tag{2}$$

$$\text{CO (g)} + \text{O(ad)-M-Al}_2\text{O}_3 \rightarrow \text{M-Al}_2\text{O}_3 + \text{CO}_2\text{ (g)} \tag{3}$$

$$\text{CO (g)} + \text{HO-M-Al}_2\text{O}_3 \rightarrow \text{M-Al}_2\text{O}_3\text{-H} + \text{CO}_2\text{ (g)} \tag{4}$$

$$\text{CO (g)} + \text{O}_2\text{(ad)-M-Al}_2\text{O}_3 \rightarrow \text{CO}_3\text{(ad)-M-Al}_2\text{O}_3 \qquad \text{carbonate formation} \tag{5}$$

$$\text{CO}_3\text{(ad)-M-Al}_2\text{O}_3 \rightarrow \text{O(ad)-M-Al}_2\text{O}_3 + \text{CO}_2\text{ (g)} \tag{6}$$

The CO oxidation mechanism was explained by the Langmuir-Hinshelwood mechanism [12,13] and the non-Langmuir-Hinshelwood mechanism [4,11], depending on the overlayer transition metals. In reaction (1), CO was adsorbed on metal site, and in reaction (2), oxygen was dissociatively adsorbed on the surface. In reaction (3), gaseous CO and surface O reacted to release $CO_2$ [12,13]. When moisture was present in the reaction, the surface OH group was plausibly formed and CO might also react with the surface metal hydroxide to form the $CO_2$ in reaction (4) [15]. On the basis of the FT-IR spectra (Supporting Information, Figure S7), surface OH groups were observed in the as-prepared samples. Therefore, reaction (4) was likely involved in the first run of $CO_2$ formation. If H was not desorbed as $H_2O$, the surface H was recycled as shown in reaction (4). Otherwise, the H was removed from the surface as gaseous $H_2O$, and, thus, the reaction (4) was diminished in the second run. Reaction (5) was also reported for surfaces such as Pt/$Al_2O_3$ [4,11]. In reaction (5), CO was adsorbed on oxygenated metal atoms to initially form carbonate. Then, the carbonate dissociated to generate $CO_2$ in reaction (6).

Photocatalytic $CO_2$ reduction products were examined for bare $Al_2O_3$ and M-$Al_2O_3$ nanosheets and are displayed in Figure 6 [39,41,42]. Major $CO_2$ reduction products were observed to be carbon monoxide (CO), methanol ($CH_3OH$), and methane ($CH_4$) with an order: $CH_4 < CH_3OH < CO$. CO was the most dominantly produced species. $CH_3OH$ showed a higher production amount compared with $CH_4$. Hydrogen ($H_2$) was additionally observed as a photocatalytic water splitting product during $CO_2$ reduction. Figure 6a plots all of the product amounts (μmol/mol = ppm) for bare $Al_2O_3$ and M-$Al_2O_3$ nanosheets. As a quick glance, Ag-$Al_2O_3$ nanosheets showed the highest amounts of $CO_2$ reduction products: 237.3 ppm for CO, 36.3 ppm for $CH_3OH$, and 30.9 ppm for $CH_4$, and Rh-$Al_2O_3$ nanosheets showed the highest $H_2$ production (20.7 ppm). For the bare $Al_2O_3$ nanosheets in Figure 6b, CO, $CH_3OH$, and $CH_4$ were observed to be 107.5 ppm, 29.6 ppm, and 19.5 ppm, respectively. No $H_2$ was detected. CO reduction yields (μmol/mol) in different groups of 9, 10, and 11, and with different units (μmol/g), are provided in the Supporting Information, Figures S8 and S9, respectively.

For bare $Al_2O_3$, the selectivities for CO, $CH_3OH$, and $CH_4$ were estimated to be 68.6%, 18.9%, and 12.5%, respectively. Upon Co- and Cu-loading, $CH_4$ and $H_2$ showed meaningful (>25%) enhancements. However, the amounts of CO and $CH_3OH$ showed no critical change. CO, $CH_3OH$, and $CH_4$ productions were enhanced by 28%, 17%, and 24% upon Ni-loading. CO was increased by 2.2× upon loading Ag in Figure 6c. $CH_3OH$ and $CH_4$ were also increased by 1.23× and 1.58×, respectively, upon loading Ag. Rh and Pd-loadings had a smaller effect on the CO production relative to the bare support. $CH_3OH$ and $CH_4$ productions were not meaningfully enhanced by Rh- and Pd-loadings. Instead, interestingly the $H_2$ production was commonly observed in these metal-loadings. For Ir, Pt, and Au elements in period 6, CO productions were all decreased by metal-loadings. $CH_3OH$ productions were somewhat increased by 19% and 16% upon loading of Pt and Au, respectively. The $CH_4$ production was only increased upon loading Pt relative to the bare substrate.

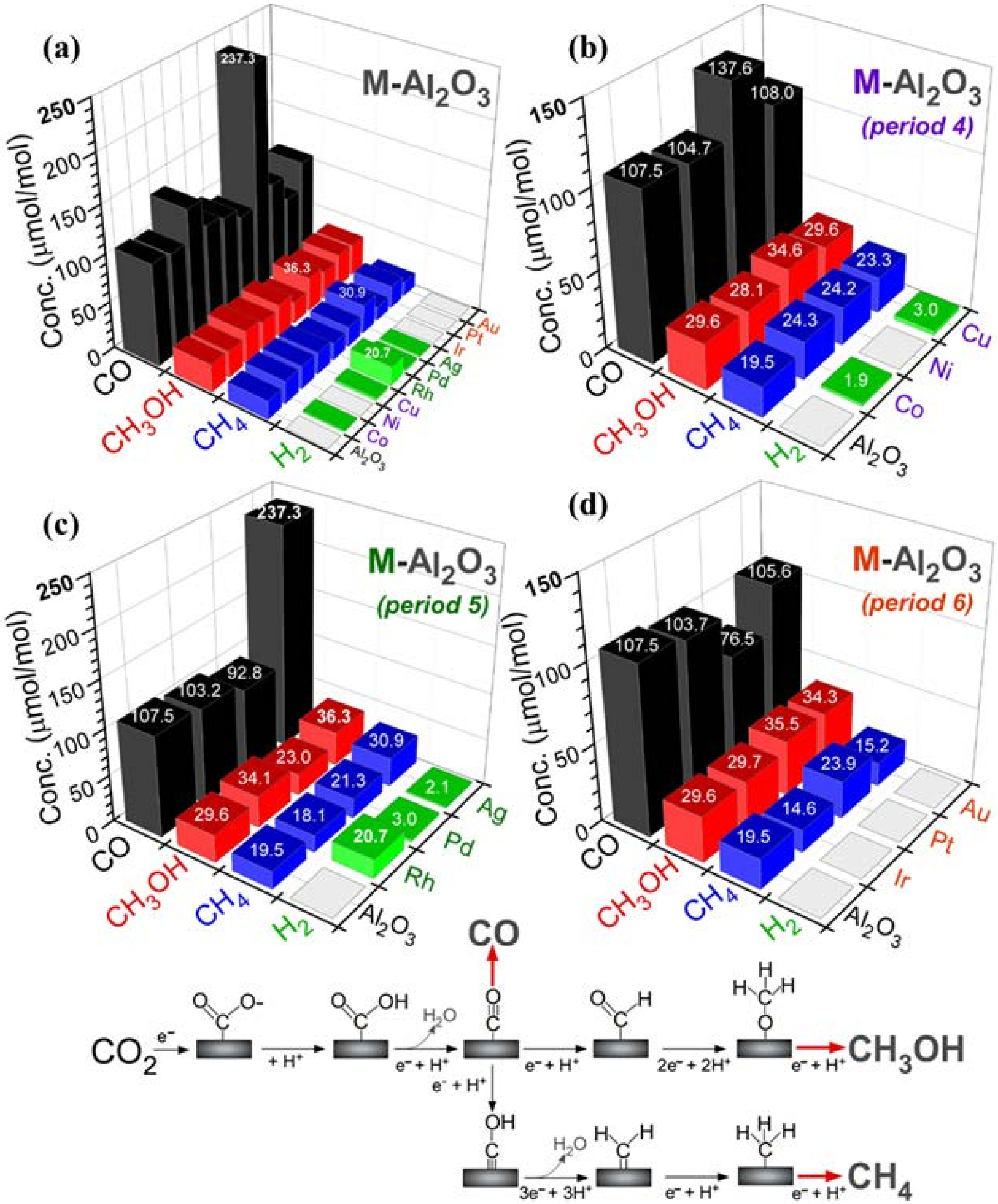

**Figure 6.** $CO_2$ reduction CO, $CH_4$, and $CH_3OH$ yields (µmol/mol) over bare and M-loaded $Al_2O_3$ nanosheets (**a**), (Co, Ni, and Cu)-$Al_2O_3$ (**b**), (Rh, Pd, and Ag)-$Al_2O_3$ (**c**), (Ir, Pt, and Au)-$Al_2O_3$ (**d**), and $CO_2$ reduction mechanism.

For $H_2$ production, Ag, Pd, and Rh (in period 5) metals commonly showed $H_2$ productions with amounts of 2.1 ppm, 3.0 ppm, and 20.7 ppm, respectively. For the metals of Co, Ni, and Cu (in period 4), the $H_2$ production amounts were observed to be 1.9 ppm, 0 ppm, and 3.0 ppm, respectively. That is, Ni showed no $H_2$ production. The metals of Au, Pt, and Ir in period 6 commonly showed no $H_2$ production at all. The Rh-$Al_2O_3$ nanosheets predominantly showed the highest $H_2$ production with an amount of 20.7 ppm.

The photocatalytic $CO_2$ reduction mechanism is generally written as $xCO_2 + yH^+ + ze^- \rightarrow C_aH_bO_c$ products + $dH_2O$ [41,42]. Electrons ($e^-$) and holes ($h^+$) were generated under UVC irradiation in reaction (7). $H^+$ ion was generated via the reactions in (8)–(11). The generation of electrons was an important factor for the multielectron processes. The mechanisms for the productions of CO (in reaction (12)), $CH_3OH$ (in reaction (13)), and $CH_4$ (in reaction (14)) are written as below and shown in Figure 6 [38,39].

$$\text{Al oxides} + \text{UVC} \rightarrow \text{Al oxides } (e^- + h^+) \tag{7}$$

$$H_2O \rightarrow H^+ + OH \tag{8}$$

$$OH^- + h^+ \rightarrow \bullet OH \tag{9}$$

$$\bullet OH + H_2O + 3h^+ \rightarrow O_2 + 3H^+ \tag{10}$$

$$H^+ + e^- \rightarrow 1/2H_2 \tag{11}$$

$$CO_2 + 2H^+ + 2e^- \rightarrow CO + H_2O, -0.530 \text{ V vs. standard hydrogen electrode (SHE)} \tag{12}$$

$$CO_2 + 6H^+ + 6e^- \rightarrow CH_3OH + H_2O, -0.380 \text{ V vs. SHE} \tag{13}$$

$$CO_2 + 8H^+ + 8e^- \rightarrow CH_4 + 2H_2O, -0.240 \text{ V vs. SHE} \tag{14}$$

These reaction channels were closely spaced in free energy change, and, thus, the hydrogen production channel ($H^+ + e^- \rightarrow 1/2H_2$, −0.42 V vs. SHE) occurred competitively. In the mechanism, $CO_2$ was initially adsorbed to form COOH. The COOH was then attacked by $H^+$ and $e^-$ to generate gaseous CO. The CO production channel was only enhanced by loading Ag or Ni on $Al_2O_3$ support. $CH_3OH$ production was likely formed when surface $CO_{ad}$ underwent step-wise hydrogenation. This production was enhanced by loading Ni, Rh, Ag, Pt, or Au on $Al_2O_3$ support. $CH_4$ production was formed via C–O bond scission of hydrogenated ≡C-OH and new C-H bond formation. This production was somewhat enhanced by loading Co, Ni, Cu, Ag, or Pt. The present pre-screening tests need further investigations to understand the detailed roles of the overlayer elements, with the aid of density functional theory.

## 4. Conclusions

In summary, γ-$Al_2O_3$ nanosheets were prepared by the solvothermal method followed by thermal calcination at 600 °C for 2 h. Transition metals (M = Co, Ni, Cu, Rh, Pd, Ag, Ir, Pt, and Au) were loaded on $Al_2O_3$ nanosheet supports, and their thermal CO oxidation and photocatalytic $CO_2$ reduction activities were fully tested.

The thermal CO oxidation activity showed the order of Ni < Co < Au < Cu < Ag << Pd < Pt < Ir < Rh in the first run, and Ni < Au < Ag < Cu < Co << Ir < Pt ≈ Pd < Rh in the second run. The Au, Ag, Co, Ni, and Cu elements reduced the catalytic activity on the $Al_2O_3$ support. CO oxidation activity was greatly enhanced by the loading of Ir, Pt, Pd, and Rh elements. Rh-$Al_2O_3$ nanosheets showed the highest CO oxidation activity with onset temperatures of 135 °C and 172 °C for the first and the second runs, respectively.

Photocatalytic $CO_2$ reduction experiments were also performed to show that CO, $CH_3OH$, and $CH_4$ were common products with an order of $CH_4$ (14.6–30.9 ppm range) < $CH_3OH$ (23.0–36.3 ppm range) << CO (76.5–237.3 ppm range). The highest performance was achieved after Ag-loadings with yields of 237.3 ppm for CO, 36.3 ppm for $CH_3OH$, and 30.9 ppm for $CH_4$, corresponding to 2.2×, 1.2×, and 1.6× enhancements, respectively, compared with those for the bare $Al_2O_3$. CO production was substantially decreased by the loading of Pd and Pt. Hydrogen production was enhanced by Rh-loadings with a yield of 20.7 ppm. Conclusively, Rh-$Al_2O_3$ and Ag-$Al_2O_3$ showed the best thermal CO oxidation and photocatalytic $CO_2$ reduction performances, respectively, among Co, Ni, Cu, Rh, Pd, Ag, Ir, Pt, and Au element loadings.

The present pre-screening test results could be a useful quick guide for the selection of overlayer transition metals in the groups of 9, 10, and 11 when $Al_2O_3$ is used as a support catalyst material. It also enriched the understanding of the role of an overlayer transition metal.

**Supplementary Materials:** The following are available online at https://www.mdpi.com/article/10.3390/nano11051278/s1, Figure S1: Scanning electron microscope (SEM) images for M-loaded $Al_2O_3$ nanosheets, Figure S2: Photos for M-loaded $Al_2O_3$ nanosheets, Figure S3: Optical microscope images for $Al_2O_3$ and M-loaded $Al_2O_3$ nanosheets, Figure S4: Transmission electron microscopic (TEM) and high-resolution TEM (HRTEM) images of Co-$Al_2O_3$ nanosheets, Figure S5: First and second CO oxidation profiles for $Al_2O_3$ and M-loaded $Al_2O_3$ nanosheets, Figure S6: Survey, C 1s, Al 2p, and O 1s profile for bare and M-$Al_2O_3$ nanosheets, Figure S7: FT-IR spectra for $Al_2O_3$ and M-loaded $Al_2O_3$ nanosheets before and after CO oxidation, Figure S8: $CO_2$ reduction CO, $CH_4$, and $CH_3OH$ yields (μmol/mol) over bare and M-loaded $Al_2O_3$ nanosheets, group 9: (Co, Rh and Ir)-$Al_2O_3$, group 10: (Ni, Pd and Pt)-$Al_2O_3$, and group 11: (Ir, Pt and Au)-$Al_2O_3$, Figure S9: CO, $CH_4$, and $CH_3OH$ yields (μmol/g) for over bare and M-loaded $Al_2O_3$ nanosheets, (Co, Ni and Cu)-$Al_2O_3$, (Rh, Pd and Ag)-$Al_2O_3$, (Ir, Pt and Au)-$Al_2O_3$.

**Author Contributions:** H.J.Y. performed the material synthesis, SEM, TEM, XRD, CO oxidation, and data analysis; J.H.Y. performed the $CO_2$ reduction and data analysis; S.J.P. performed the XPS experiments and data analysis; Y.S. designed the experiments and wrote the paper. All authors have read and agreed to the published version of the manuscript.

**Funding:** This research was finally supported by the National Research Foundation of Korea (NRF) grant funded by the Korea government (MEST; 2016R1D1A3B04930123).

**Data Availability Statement:** Data are available in the main text.

**Conflicts of Interest:** The authors declare no conflict of interest.

## References

1. Chen, Y.; Feng, Y.X.; Li, L.; Liu, J.Y.; Pan, X.L.; Liu, W.; Wei, F.F.; Cui, Y.T.; Qiao, B.T.; Sun, X.C.; et al. Identification of active sites on high-performance Pt/$Al_2O_3$ catalyst for cryogenic CO oxidation. *ACS Catal.* **2020**, *10*, 8815–8824. [CrossRef]
2. Lou, Y.; Liu, J. CO oxidation on metal oxide supported single Pt atoms: The role of the support. *Indus. Eng. Chem. Res.* **2017**, *56*, 6916–6925. [CrossRef]
3. Hazlett, M.J.; Moses-Debusk, M.; Parks, J.E.; Allard, L.F.; Epling, W.S. Kinetic and mechanistic study of bimetallic Pt-Pd/$Al_2O_3$ catalysts for CO and $C_3H_6$ oxidation. *Appl. Catal. B* **2017**, *202*, 404–417. [CrossRef]
4. Newton, M.A.; Ferri, D.; Smolentsev, G.; Marchionni, V.; Nachtegaal, M. Kinetic Studies of the Pt Carbonate-Mediated, Room-Temperature Oxidation of Carbon Monoxide by Oxygen over Pt/$Al_2O_3$ Using Combined, Time-Resolved XAFS, DRIFTS, and Mass Spectrometry. *J. Am. Chem. Soc.* **2016**, *138*, 13930–13940. [CrossRef]
5. Zhang, Z.; Zhu, Y.; Asakura, H.; Zhang, B.; Zhang, J.; Zhou, M.; Han, Y.; Tanaka, T.; Wang, A.; Zhang, T.; et al. Thermally stable single atom Pt/m-$Al_2O_3$ for selective hydrogenation and CO oxidation. *Nat. Commun.* **2017**, *8*, 16100. [CrossRef] [PubMed]
6. Ananth, A.; Jeong, R.H.; Boo, J.-H. Preparation, characterization and CO oxidation performance of $Ag_2O/\gamma$-$Al_2O_3$ and ($Ag_2O$+$RuO_2$)/$\gamma$-$Al_2O_3$ catalysts. *Surfaces* **2020**, *3*, 251–264. [CrossRef]
7. Yang, T.; Fukuda, R.; Hosokawa, S.; Tanaka, T.; Sakaki, S.; Ehara, M. A theoretical investigation on CO oxidation by single-atom catalysts $M_1$ /$\gamma$-$Al_2O_3$ (M = Pd, Fe, Co, and Ni). *ChemCatChem* **2017**, *9*, 1222–1229. [CrossRef]
8. Gao, H. CO oxidation mechanism on the $\gamma$-$Al_2O_3$ supported single Pt atom: First principle study. *Appl. Surf. Sci.* **2016**, *379*, 347–357. [CrossRef]
9. Li, Q.; Wei, Y.; Sa, R.; Ma, Z.; Wu, K. A novel $Pd_3O_9$@$Al_2O_3$ catalyst under a hydroxylated effect: High activity in the CO oxidation reaction. *Phys. Chem. Chem. Phys.* **2015**, *17*, 32140–32148. [CrossRef] [PubMed]
10. Li, Z.-Y.; Yuan, Z.; Li, X.-N.; Zhao, Y.-X.; He, S.-G. CO oxidation catalyzed by single gold atoms supported on aluminum oxide clusters. *J. Am. Chem. Soc.* **2014**, *136*, 14307–14313. [CrossRef]
11. Moses-DeBusk, M.; Yoon, M.; Allard, L.F.; Mullins, D.R.; Wu, Z.; Yang, X.; Veith, G.; Stocks, G.M.; Narula, C.K. CO oxidation on supported single Pt atoms: Experimental and ab initio density functional studies of CO interaction with Pt atom on θ-$Al_2O_3$ (010) surface. *J. Am. Chem. Soc.* **2013**, *135*, 12634–12645. [CrossRef] [PubMed]
12. Zhou, Y.; Wang, Z.; Liu, C. Perspective on CO oxidation over Pd-based catalysts. *Catal. Sci. Technol.* **2015**, *5*, 69–81. [CrossRef]

13. Satsuma, A.; Osaki, K.; Yanagihara, M.; Ohyama, J.; Shimizu, K. Activity controlling factors for low-temperature oxidation of CO over supported Pd catalysts. *Appl. Catal. B* **2013**, *132–133*, 511–518. [CrossRef]
14. Haneda, M.; Todo, M.; Nakamura, Y.; Hattori, M. Effect of Pd dispersion on the catalytic activity of Pd/$Al_2O_3$ for $C_3H_6$ and CO oxidation. *Catal. Today* **2017**, *281*, 447–453. [CrossRef]
15. Gavril, D. CO oxidation on nanosized Au/$Al_2O_3$ by surface hydroxyl groups and in the absence of $O_2$, studied by inverse gas chromatography. *Catal. Today* **2015**, *244*, 36–46. [CrossRef]
16. Han, S.W.; Kim, D.H.; Jeong, M.-G.; Park, K.J.; Kim, Y.D. CO oxidation catalyzed by NiO supported on mesoporous $Al_2O_3$ at room temperature. *Chem. Eng. J.* **2016**, *283*, 992–998. [CrossRef]
17. Kwak, J.H.; Hu, J.; Mei, D.; Yi, C.-W.; Kim, D.H.; Peden, C.H.F.; Allard, L.F.; Szanyi, J. Coordinatively Unsaturated $Al^{3+}$ Centers as Binding Sites for Active Catalyst Phases of Platinum on $\gamma$-$Al_2O_3$. *Science* **2009**, *325*, 1670–1673. [CrossRef]
18. Shen, Y.; Lu, G.; Guo, Y.; Wang, Y. A synthesis of high-efficiency Pd-Cu-$Cl_x$/$Al_2O_3$ catalyst for low temperature CO oxidation. *Chem. Commun.* **2010**, *46*, 8433–8435. [CrossRef]
19. Gribov, E.N.; Zavorotynska, O.; Agostini, G.; Vitillo, J.G.; Ricchiardi, G.; Spoto, G.; Zecchina, A. FTIR spectroscopy and thermodynamics of CO and $H_2$ adsorbed on $\gamma$-, $\delta$- and $\alpha$-$Al_2O_3$. *Phys. Chem. Chem. Phys.* **2010**, *12*, 6474–6482. [CrossRef]
20. Kwak, J.H.; Kovarik, L.; Szanyi, J. $CO_2$ reduction on supported Ru/$Al_2O_3$ catalysts: Cluster size dependence of product selectivity. *ACS Catal.* **2013**, *3*, 2449–2455. [CrossRef]
21. Zhao, H.; Zheng, X.; Feng, X.; Li, Y. $CO_2$ reduction by plasmonic Au nanoparticle-decorated $TiO_2$ photocatalyst with an ultrathin $Al_2O_3$ interlayer. *J. Phys. Chem. C* **2018**, *122*, 18949–18956. [CrossRef]
22. Zhao, H.; Chen, J.; Rao, G.; Deng, W.; Li, Y. Enhancing photocatalytic $CO_2$ reduction by coating an ultrathin $Al_2O_3$ layer on oxygen deficient $TiO_2$ nanorods through atomic layer deposition. *Appl. Surf. Sci.* **2017**, *404*, 49–56. [CrossRef]
23. Wu, S.; Li, Y.; Zhang, Q.; Hu, Q.; Wu, J.; Zhou, C.; Zhao, X. Formation of NiCo alloy nanoparticles on Co doped $Al_2O_3$ leads to high fuel production rate, large light-to-fuel efficiency, and excellent durability for photothermocatalytic $CO_2$ reduction. *Adv. Energy Mater.* **2020**, *10*, 2002602. [CrossRef]
24. Méndez-Mateos, D.; Barrio, V.L.; Requies, J.M.; Cambra, J.F. Effect of the addition of alkaline earth and lanthanide metals for the modification of the alumina support in Ni and Ru catalysts in $CO_2$ methanation. *Catalysts* **2021**, *11*, 353. [CrossRef]
25. Mihet, M.; Lazar, M.D. Methanation of $CO_2$ on Ni/$\gamma$-$Al_2O_3$: Influence of Pt, Pd or Rh promotion. *Catal. Today* **2018**, *306*, 294–299. [CrossRef]
26. Liang, C.; Hu, X.; Wei, T.; Jia, P.; Zhang, Z.; Dong, D.; Zhang, S.; Liu, Q.; Hu, G. Methanation of $CO_2$ over Ni/$Al_2O_3$ modified with alkaline earth metals: Impacts of oxygen vacancies on catalytic activity. *Int. J. Hydrog. Energy* **2019**, *44*, 8197–8213. [CrossRef]
27. Chein, R.-Y.; Wang, C.-C. Experimental study on $CO_2$ methanation over Ni/$Al_2O_3$, Ru/$Al_2O_3$, and Ru-Ni/$Al_2O_3$ catalysts. *Catalysts* **2020**, *10*, 1112. [CrossRef]
28. Lou, Y.; Liu, J. A highly active Pt–Fe/$\gamma$-$Al_2O_3$ catalyst for preferential oxidation of CO in excess of $H_2$ with a wide operation temperature window. *Chem. Commun.* **2017**, *53*, 9020–9023. [CrossRef]
29. Chen, Y.; Lin, J.; Li, L.; Pan, X.; Wang, X.; Zhang, T. Local structure of Pt species dictates remarkable performance on Pt/$Al_2O_3$ for preferential oxidation of CO in $H_2$. *Appl. Catal. B* **2021**, *282*, 119588. [CrossRef]
30. Han, D.; Lee, D. Morphology controlled synthesis of $\gamma$-$Al_2O_3$ nano-crystallites in Al@$Al_2O_3$ core–shell micro-architectures by interfacial hydrothermal reactions of Al metal substrates. *Nanomaterials* **2021**, *11*, 310. [CrossRef] [PubMed]
31. Lee, S.; Kang, J.S.; Leung, K.T.; Kim, S.K.; Sohn, Y. Magnetic Ni-Co alloys induced by water gas shift reaction, Ni-Co oxides by CO oxidation and their supercapacitor applications. *Appl. Surf. Sci.* **2016**, *386*, 393–404. [CrossRef]
32. NIST Standard Reference Database 20, Version 4.1. 2012. Available online: https://srdata.nist.gov/xps/ (accessed on 1 March 2021).
33. Akhavan, O.; Azimirad, R.; Safa, S.; Hasani, E. CuO/Cu$(OH)_2$ Hierarchical nanostructures as bactericidal photocatalysts. *J. Mater. Chem.* **2011**, *21*, 9634–9640. [CrossRef]
34. Reneme, Y.; Dhainaut, F.; Trentesaux, M.; Ravanbakhsh, B.; Granger, P.; Dujardin, C.; Gengembre, L.; De Cola, P.L. XPS investigation of surface changes during thermal aging of natural gas vehicle catalysts: Influence of Rh addition to Pd. *Surf. Interface Anal.* **2010**, *42*, 530–535. [CrossRef]
35. Ivanova, A.S.; Slavinskaya, E.M.; Gulyaev, R.V.; Zaikovskii, V.I.; Stonkus, O.A.; Danilova, I.G.; Plyasova, L.M.; Polukhina, I.A.; Boronin, A.I. Metal-support interactions in Pt/$Al_2O_3$ and Pd/$Al_2O_3$ catalysts for CO oxidation. *Appl. Catal. B* **2010**, *97*, 57–71. [CrossRef]
36. Kang, J.G.; Sohn, Y. Interfacial nature of Ag nanoparticles supported on $TiO_2$ photocatalysts. *J. Mater. Sci.* **2012**, *47*, 824–832. [CrossRef]
37. Freakley, S.J.; Ruiz-Esquius, J.; Morgan, D.J. The X-ray photoelectron spectra of Ir, $IrO_2$ and $IrCl_3$ revisited. *Surf. Interface Anal.* **2017**, *49*, 794–799. [CrossRef]
38. Yoon, H.J.; Kim, S.K.; Lee, S.W.; Sohn, Y. Stalagmite Al$(OH)_3$ growth on aluminum foil surface by catalytic $CO_2$ reduction with $H_2O$. *Appl. Surf. Sci.* **2018**, *450*, 85–90. [CrossRef]
39. Yang, J.H.; Park, S.J.; Rhee, C.K.; Sohn, Y. Photocatalytic $CO_2$ reduction and electrocatalytic $H_2$ evolution over Pt(0,II,IV)-loaded oxidized Ti sheets. *Nanomaterials* **2020**, *10*, 1909. [CrossRef]
40. Filatova, E.O.; Konashuk, A.S. Interpretation of the changing the band gap of $Al_2O_3$ depending on its crystalline form: Connection with different local symmetries. *J. Phys. Chem. C* **2015**, *119*, 20755–20761. [CrossRef]

41. Sun, Z.; Ma, T.; Tao, H.; Fan, Q.; Han, B. Fundamentals and challenges of electrochemical $CO_2$ reduction using two-dimensional materials. *Chem* **2017**, *3*, 560–587. [CrossRef]
42. Sohn, Y.; Huang, W.; Taghipour, F. Recent progress and perspectives in the photocatalytic $CO_2$ reduction of Ti-oxide-based nanomaterials. *Appl. Surf. Sci.* **2017**, *396*, 1696–1711. [CrossRef]